Phase Field Simulations of Intermetallic Compound Growth during Soldering Reactions

J.Y. HUH,[1,4] K.K. HONG,[1] Y.B. KIM,[2] and K.T. KIM[3]

1.—Division of Materials Science and Engineering, Korea University, Seoul 137-713, Korea. 2.—Samsung Electro-Mechanics Co., Ltd., Suwon 442-743, Korea. 3.—Samsung Electronics Co., Ltd., Yongin 449-711, Korea. 4.—E-mail: jyhuh@korea.ac.kr

Phase field simulations of the microstructural evolution of the intermetallic compound (IMC) layer formed during isothermal soldering reactions between Sn-Cu solder alloys and a Cu substrate are presented. The simulation accounts for the fast grain boundary (GB) diffusion in the IMC layer, the concurrent IMC grain coarsening along with the IMC layer growth, and the dissolution of Cu from the substrate and IMC layer. The simulation results support the previous suggestions that the growth kinetics of the IMC layer during soldering is predominantly governed by the fast GB diffusion and the concurrent coarsening rate of the IMC grains. The IMC grain coarsening is initiated by a competitive growth of the IMC grains at the solder/IMC interface. It is also shown that the dissolution of Cu into an unsaturated solder reduces the coarsening rate of the IMC grains, consequently decreasing the temporal growth exponent of the IMC layer.

Key words: Soldering, phase field model, intermetallic compound (IMC) growth, grain boundary (GB) diffusion, grain coarsening

INTRODUCTION

Interface reactions occur readily when a molten metal is in contact with a compatible solid metal. Such reactions involve interdiffusion between the liquid and solid metals and often result in the formation and growth of intermetallic compounds (IMCs) at the interface. During the soldering process, IMCs form and grow at the interface between a molten Sn-based solder and a metallic substrate.[1,2] The formation of an IMC layer is essential to ensure the metallurgical bonding at the solder joint. However, excessive growth of the IMC layer is known to be detrimental for the mechanical properties of solder joints, such as fatigue properties and shear strengths, due to the brittle nature of IMCs.[3–6]

The growth and microstructural evolution of the IMC layer during soldering reactions has received renewed attention lately along with the technological trend toward miniaturization of electronic packages and the necessity to find Pb-free solders. The IMC layer growth is of concern when soldering thin-film metallizations used in microelectronic device packages, since the consumption of thin metal films by IMC growth deteriorates solderability.[7–9] The microstructure of the IMC layer formed during the soldering process is also of concern, since it influences the growth kinetics of the IMC layer in subsequent aging and consequently the solder joint reliability.[10, 11]

When Sn-based solders bond with a Cu substrate, two IMC layers, consisting of Cu_6Sn_5 (η) and Cu_3Sn (ε), can form between the solder and the Cu substrate. Only the Cu_6Sn_5 layer is usually formed at the solder/substrate interface under typical soldering conditions employed in electronic packaging. The growth kinetics of the Cu_6Sn_5 layer during isothermal soldering is often modeled with a power law dependence of the layer thickness (W) on the soldering time (t), $W = k \times t^n$. The temporal growth exponent, n, has been observed to be in the range between 0.25 and 0.37, depending on solder alloys, solder volume, and soldering process parameters.[12–14] These low values of the temporal growth exponent, compared to $n = 0.5$ for the parabolic growth law, have been attributed[13–16] to (1) the dominant diffusion mechanism for the IMC layer

(Received April 12, 2004; accepted May 09, 2004)

growth, which is the fast diffusion through the grain boundary (GB) of the IMC layer (or through the liquid solder channel in between IMC grains); and (2) the concurrent coarsening of the IMC grains as the IMC layer grows, which results in a gradual reduction of the fast diffusion paths.

The purpose of this work is twofold. The first is the development of a phase field model to simulate the microstructural evolution of the IMC layer formed by the interface reaction. The phase field model accounts for the fast GB diffusion in the IMC layer and the IMC grain coarsening driven by the interface curvature effect. The second is to examine the effects of the fast GB diffusion and concurrent coarsening of the IMC grains on the growth kinetics of the IMC layer formed by the soldering reaction between Sn-Cu solders and a Cu substrate at 250ºC. For this purpose, we simulated the IMC layer evolution by employing different values of the GB diffusivity and the interface energy between the liquid solder and IMC layer. Simulations were also carried out by varying the initial Cu content in the solder (i.e., from nearly pure Sn to Cu-saturated Sn-Cu) to examine the effect of the Cu dissolution into the solder on the IMC layer growth.

PHASE FIELD MODEL

We consider an isothermal Cu-Sn binary system that is composed of three phases: a Sn-rich liquid solder (L), a Cu-rich solid substrate (α), and an IMC layer of Cu_6Sn_5 (η) formed between the liquid solder and the solid substrate. The IMC layer is polycrystalline consisting of N – 2 grains that are differentiated only by the crystallographic orientation. The spatial distribution of the liquid solder, the substrate, and the η-IMC grains in the system at a given time (t) is mathematically expressed by using N arrays of phase fields, $\phi_i(\vec{x},t)$ (; i = 1, …, N). The phase field variables in this model are defined in such a way that ϕ_l, ϕ_N, and ϕ_j(; j = 2, …, N–1) correspond to the local phase fractions of the α and liquid phases, and the jth grain of the η-IMC layer, respectively. The region where $\phi_i = 1$ corresponds to the bulk of i phase or ith η grain, and the region where ϕ_i changes continuously within $0 < \phi_i < 1$ corresponds to the interface (or GB) adjacent to i phase (or ith η grain). In this way, the interface is considered as a finite region of a mixture of different phases or grains. Therefore, the N phase field variables at any position in the system are subjected to the constraint:

$$\sum_{i=1}^{N} \phi_i(\vec{x},t) = 1 \tag{1}$$

Energetics

The total free energy of the system with spatial inhomogeneities in the composition of Sn, c, and the phase field variables, ϕ_i (; i = 1, …, N), is written as a function of these variables in the following form[17,18] of a volume integral:

$$F = \int_V \left[\sum_{i=1}^{N} \left\{ \phi_i f_i(c_i) + \sum_{j=i+1}^{N} \left(-\frac{\varepsilon_{ij}^2}{2} \nabla\phi_i . \nabla\phi_j + \omega_{ij}\, \phi_i \phi_j \right) \right\} - \lambda_\phi \left(\sum_{i=1}^{N} \phi_i - 1 \right) \right] dV \tag{2}$$

where λ_ϕ is the Lagrange multiplier for the constraint Eq. 1, $f_i(c_i)$ is the chemical free energy density of i phase that depends on the phase composition c_i, and ε_{ij} and ω_{ij} are the (constant) gradient energy coefficient and the positive (constant) barrier height, respectively, that are associated with the interfacial energy between $\phi_i = 1$ and $\phi_j = 1$ phases (or grains). Since only the values of ϕ_i in the range of $0 \le \phi_i \le 1$ are physical, we set $\omega_{ij} = \infty$ for either $\phi_i > 1$ ($\phi_j < 0$) or $\phi_i < 0$ ($\phi_j > 1$), by which the term $\omega_{ij}\phi_i\phi_j$ in Eq. 2 may be called a "double obstacle potential,"[19] compared to the conventional double well potential $\omega_{ij}\phi_i^2\phi_j^2$. The advantage of using the double obstacle potential instead of the double well potential is that the temporal evolution of the phase fields can be computed only for the well-defined, finite region of the interface.

As mentioned above, the interface region is considered as a mixture of the phases of which phase field variables are nonzero. Following Kim et al.,[20] the coexisting phases at a position in the interface region are assumed to have an identical value to the diffusion potential[21] that is defined as the difference between the chemical potentials of constituent species:

$$\frac{\partial f_1}{\partial c_1} = \frac{\partial f_2}{\partial c_2} = \ldots = \frac{\partial f_N}{\partial c_N} \equiv f'(c, \phi_i) \tag{3}$$

The phase compositions c_i of the coexisting phases are also subjected to local mass conservation:

$$\sum_{i=1}^{N} \phi_i(\vec{x},t)\, c_i(\vec{x},t) = c(\vec{x},t) \tag{4}$$

For a given set of c and ϕ_i (; i =1, …, N), the phase compositions of the coexisting phases can be calculated by solving Eqs. 3 and 4 simultaneously. It is noted that the assumption of Eq. 3 implies that different η grains present at a position in the GB region have the same phase compositions, i.e., $c_2(\vec{x},t) = c_3(\vec{x},t) = \ldots = c_{N-1}(\vec{x},t)$.

Evolution Equations

The evolution of the composition field $c(\vec{x},t)$ and the phase fields $\phi_i(\vec{x},t)$ (; i = 1, …, N) with time is assumed to occur in such a way that the total free energy of the system, F, decreases monotonically toward a minimum. This is guaranteed by using the Cahn–Hilliard and Cahn–Allen equations:

$$\frac{\partial c}{\partial t} = -\nabla \cdot \vec{j} \tag{5}$$

with the flux $\vec{j}$ given by

$$\vec{j} = -M_c(c, \phi_k) \nabla \left(\frac{\delta F}{\delta c} \right) \tag{6}$$

and

$$\frac{\partial \phi_i}{\partial t} = -L_i(c, \phi_k)\left(\frac{\delta F}{\delta \phi_i}\right) \quad ; i = 1, \ldots, N \tag{7}$$

where M_c and L_i are the atomic mobility and the relaxation coefficient for ϕ_i, respectively, that can be functions of c and ϕ_k(; k = 1, ..., N). After using the condition of Eq. 3 and the relationship $\sum_{i=1}^{N} \phi_i (\partial c_i/\partial c)_{\phi_j} = 1$ resulting from Eq. 4, the functional derivatives in Eqs. 6 and 7 are expressed as

$$\frac{\delta F}{\delta c} = \sum_{i=1}^{N} \phi_i \left(\frac{df_i}{dc_i}\right)\left(\frac{\partial c_i}{\partial c}\right)_{\phi_j} = f' \tag{8}$$

and

$$\frac{\delta F}{\delta \phi_i} = \sum_{j \neq i}^{N} \left\{\frac{\varepsilon_{ij}^2}{2}\nabla^2 \phi_j + \omega_{ij}\phi_j\right\} + \left\{f_i(c_i) - c_i f'\right\} - \lambda_\phi \tag{9}$$

with $\varepsilon_{ij} = \varepsilon_{ji}$ and $\omega_{ij} = \omega_{ji}$. The notation $\sum_{j \neq i}^{N}$ in Eq. 9 is used to indicate the summation from j = 1 to j = N, except for j = i.

Substituting Eq. 8 into Eq. 6 and using Eq. 4 result in the flux equation expressed in a more convenient form:[18]

$$\vec{j} = -D(\phi_k)\sum_{i=1}^{N} \phi_i \nabla c_i \tag{10}$$

where $D = M_c (\partial f'/\partial c)_{\phi_i}$ is the interdiffusion coefficient that is assumed to depend only on ϕ_k (; k = 1, …, N). Combining Eqs. 5 and 10 gives the diffusion equation

$$\frac{\partial c}{\partial t} = \nabla \cdot \left[D(\phi_i)\sum_{i=1}^{N} \phi_i \nabla c_i\right] \tag{11}$$

In contrast with the evolution of the composition field that occurs throughout the bulk of the system, the evolution of the phase fields occurs only in the interface region. We introduce a step function $s_i(\vec{x},t)$ defined in such a way that $s_i = 1$ if $\phi_i(\vec{x},t) > 0$ and $s_i = 0$ otherwise. Then, the number of coexisting phases (or grains) at a given position, p, is given by

$$p(\vec{x},t) = \sum_{i=1}^{N} s_i(\vec{x},t) \tag{12}$$

As pointed out by Steinbach and Pezzolla,[17] the use of Eq. 7 for the evolution of ϕ_i gives rise to an ambiguity in the definition of the relaxation coefficient L_i at triple (p = 3) or multiple (p > 3) junctions of interfaces. Therefore, following Reference 17, Eq. 7 is decomposed in such a way that the change of ϕ_i is attributed to the sum of the pairwise interactions between ϕ_i and nonzero ϕ_j:

$$\frac{\partial \phi_i}{\partial t} = -\frac{2}{p} s_i \sum_{j \neq i}^{N} s_j M_{ij}\left(\frac{\delta F}{\delta \phi_i} - \frac{\delta F}{\delta \phi_j}\right); i = 1, \ldots, N \tag{13}$$

where M_{ij} is the mobility (assumed constant) of the specific interface between the two phases (or grains) of $\phi_i = 1$ and $\phi_j = 1$. Using Eq. 9, Eq. 13 is recast in the following form:

$$\begin{aligned}\frac{\partial \phi_i}{\partial t} = -\frac{2}{p} s_i \sum_{j \neq i}^{N} s_j M_{ij} \Bigg[& \frac{\varepsilon_{ij}^2}{2}\left(\nabla^2 \phi_j - \nabla^2 \phi_i\right) + \omega_{ij}\left(\phi_j - \phi_i\right) \\ & + \sum_{k \neq i,j}^{N} s_k \left\{\left(\frac{\varepsilon_{ik}^2}{2} - \frac{\varepsilon_{jk}^2}{2}\right)\nabla^2 \phi_k + \left(\omega_{ik} - \omega_{jk}\right)\phi_k\right\} \\ & + \left\{\left(f_i - c_i f'\right) - \left(f_j - c_j f'\right)\right\}\Bigg]; i = 1, \ldots, N\end{aligned} \tag{14}$$

The gradient energy coefficient ε_{ij} and the barrier height ω_{ij} can be related to the interface energy σ_{ij} and the interface width w_{ij}, considering a two-phase equilibrium state of $\phi_i = 1$ and $\phi_j = 1$ phases with a planar interface. They are determined as[18]

$$\varepsilon_{ij} = \frac{\sqrt{8\sigma_{ij} w_{ij}}}{\pi} \quad \text{and} \quad \omega_{ij} = \frac{4\sigma_{ij}}{w_{ij}} \tag{15}$$

NUMERICAL PROCEDURE

Scaling of Length and Time

We assume that all the two-phase interfaces (and GBs) have the same width, i.e., $w_{ij} = \pi\varepsilon_{ij}/\sqrt{2\omega_{ij}} \equiv w$. Since there are large discrepancies in the diffusivities of individual phases in the Cu-Sn system in the literature.[22–24] we use a scaled position, $\vec{z}$, and time, τ, in the numerical procedure, which are defined by

$$\vec{z} = \vec{x}/w \quad \text{and} \quad \tau = D_L\, t/w^2 \tag{16}$$

where D_L is the interdiffusion coefficient of the liquid solder phase. Then, $D(\phi_k)$ and M_{ij} in the evolution, Eqs. 11 and 14, are replaced by the relative diffusivity, $\bar{D}(\phi_k) \equiv D(\phi_k)/D_L$, and interface mobility, $\bar{M}_{ij} \equiv M_{ij}/D_L$, respectively, in the corresponding equations employing the scaled position and time.

Simulation System

Two-dimensional simulation on the cross section of the Cu/Sn solder joint at 250ºC is performed by solving the evolution Eqs. 11 and 14 numerically using an explicit, finite-difference technique. In all cases, a nondimensional grid spacing of h = 0.25 is used, which allows each interface (or GB) to extend over four grid points. Figure 1 shows a schematic representation of the computational cell of 184 h × 90 h at the initial configuration with the η-IMC layer placed in 25 h ≤ z_2 ≤ 29 h between the liquid solder and the α-Cu substrate. The η-IMC layer initially consists of 30 rectangular grains with widths randomly sized between 4 h and 8 h. The boundary conditions for c and ϕ_i are periodic along the z_1 axis

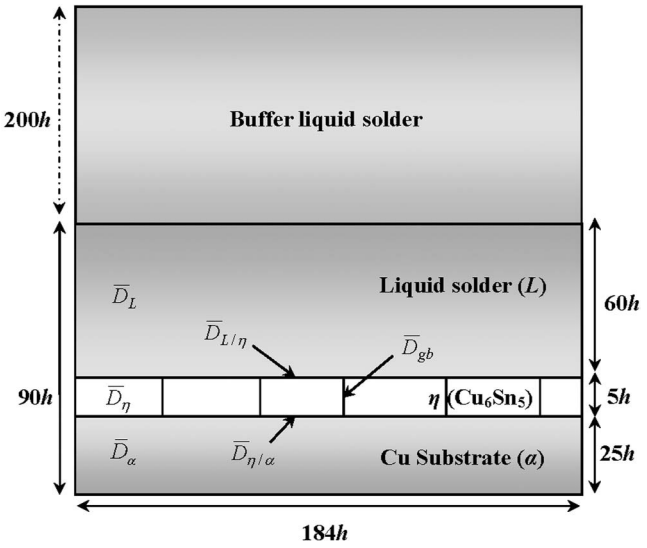

Fig. 1. Schematic representation of the computational cell of 184 h × 90 h, where h is the grid spacing. The η-IMC layer consisting of 30 grains with a uniform thickness of 5 h was initially placed in between the liquid solder and the substrate. In order to account for a larger volume of the liquid solder, an additional buffer solder of 184 h × 200 h was located at the top of the computational cell, the composition of which was initially the same as that of the solder in the computational cell and changed with time due to the diffusion flux at the top of the computation cell.

and of a Neumann type (their spatial derivatives being equal to zero) at the bottom surface ($z_2 = 0$).

Since the liquid solder volume in the computational cell is rather small compared to typical solder joint systems employed in microelectronic packaging, we put an additional buffer solder region of 184 h × 200 h at the top ($z_2 = 90$ h) of the computational cell. The composition of the buffer region is initially the same as that of the solder in the computational solder. The average composition of the buffer region changes with time and is calculated from the diffusion fluxes at the top surface of the computational cell. The average composition of the buffer region is in turn used as the boundary condition at the top surface ($z_2 = 90$ h) for the calculation of the composition field at the next time-step. Since the diffusion Eq. 11 is not solved for the buffer region, use of the buffer region significantly saves computation time while accounting for a large solder volume.

The chemical free energy densities (f_α, f_η, and f_L) of individual phases were obtained from the CALPHAD method[25] and are summarized in Table I. We assumed that all the phases have the same molar volume, V_m, and that, in order to allow a solubility range in the η-IMC phase, f_η is a parabolic function of composition. The chemical free energy densities given in Table I result in the equilibrium phase compositions at 250ºC: $c_\alpha^{\alpha\eta} \approx 0.1954$, $c_\eta^{\eta\alpha} \approx 0.380$, $c_\eta^{\eta L} \approx 0.441$, and $c_L^{L\eta} \approx 0.9769$, where $c_\alpha^{\alpha\eta}$ is the equilibrium composition of the α phase at the α/η interface and the other terms are defined correspondingly. The initial compositions of the substrate and η-IMC layer are taken to be uniform as $c_\alpha(\vec{z},0) = 0.002$ and $c_\eta(\vec{z},0) = 0.4105$, respectively. The initial composition of the liquid solder phase is chosen to be either $c_L(\vec{z},0) = c_L^{L\eta}$ corresponding to a Cu-saturated solder, or $c_L(\vec{z},0) = c_L^{L\eta} + 0.02$, corresponding to a nearly pure Sn solder.

Numerical Method

The simulations are carried out by solving Eqs. 11 and 14 numerically using an explicit, finite-difference technique consisting of two grids. The first grid with a nondimensional grid spacing of h = 0.25, as mentioned above, is used to define the composition and phase fields. The second grid with nodal points located at the midpoints of the first grid is used to define the diffusion flux. The Euler method with a nondimensional time-step $\Delta\tau = 0.0125$ is used for the time integration.

In the simulation, we take explicitly into account the fast diffusion through the interfaces or GBs. The fluxes, given by Eq. 10, at the nodal points of the second grid are first computed when solving the diffusion equation Eq. 11. Five-point, central difference formulae are used for the spatial derivatives. For $D(\phi_i)$ at a nodal point of the second grid, ϕ_i (; i = 1, …, N) values at the nodal point are first determined using the Lagrange interpolation on the four neighboring nodal points of the first grid. $D(\phi_i)$ is then defined in the following way: $D(\phi_i) = D_\alpha$ if $\phi_1 > 0.8$, $D(\phi_i) = D_L$ if $\phi_N > 0.8$, $D(\phi_i) = D_\eta$ if any $\phi_j > 0.8$ (;j = 2,…, N–1), $D(\phi_i) = D_{L/\eta}$ if $0.2 \le \phi_N \le 0.8$, $D(\phi_i) = D_{\eta/\alpha}$ if $\phi_N < 0.2$ and $(1-\phi_j)/2 < \phi_1 \le 0.8$ (; j = 2,…, N–1), and $D(\phi_i) = D_{gb}$ otherwise. The terms D_L, $D_{L/\eta}$, $D_{\eta/\alpha}$, and D_{gb} denote the bulk diffusivity of the liquid phase, the interface diffusivities along the L/η and η/α interfaces, and the GB diffusivity of the η-IMC layer, respectively. The relative diffusivities and other material parameters employed in the numerical calculation are summarized in Table II.

Finally, we note in the numerical treatment of Eq. 14 that the step function s_i at a nodal point of

Table I. Chemical Free Energy Densities at T = 523 K[25]

$f_\alpha \cdot V_m$ (J/mole)	$(1-c)G_{Cu}^{o\alpha} + cG_{Sn}^{o\alpha} + RT[(1-c)\ln(1-c) + c\ln c] + c(1-c)[L_0^\alpha + L_1^\alpha(1-2c)]$
	$G_{Cu}^{o\alpha} = -1.9073 \times 10^4$, $G_{Sn}^{o\alpha} = -2.7281 \times 10^4$, $L_0^\alpha = -1.1448 \times 10^4$, $L_1^\alpha = -1.1694 \times 10^4$
$f_\eta \cdot V_m$ (J/mole)	$2.0 \times 10^5 (c - 0.435)^2 + 0.545G_{Cu}^{o\alpha} + 0.455G_{Sn}^{SER} - 6869.5 - 0.1589T$
	$G_{Cu}^{o\alpha} = -1.9073 \times 10^4$, $G_{Sn}^{SER} = 3.4616 \times 10^5$
$f_L \cdot V_m$ (J/mole)	$(1-c)G_{Cu}^{oL} + cG_{Sn}^{oL} + RT[(1-c)\ln(1-c) + c\ln c] + c(1-c)[L_0^L + L_1^L(1-2c) + L_2^L(1-4c+4c^2)]$
	$G_{Cu}^{oL} = -1.1083 \times 10^4$, $G_{Sn}^{oL} = -2.8963 \times 10^4$, $L_0^L = -1.0487 \times 10^4$, $L_1^L = -1.8198 \times 10^4$, $L_2^L = -10528.4$
V_m (m^3/mole)	16.29×10^{-6}

Table II. Material Parameters Employed in the Present Study

$\bar{D}_{\alpha}$	1.0×10^{-6}
$\bar{D}_{\eta}$	2.0×10^{-5}
$\bar{D}_{L/\eta}$	2.0×10^{-1}
$\bar{D}_{\eta/\alpha}$	2.0×10^{-3}
$\bar{D}_{gb}$	2.0×10^{-2}
$\sigma_{L/\eta}$ (J/m^2)	0.1
$\sigma_{\eta/\alpha} = \sigma_{gb}$ (J/m^2)	0.3
$\bar{M}_{L/\eta}$	1.0×10^{6}
$\bar{M}_{\eta/\alpha} = \bar{M}_{gb}$	7.0×10^{4}

the first grid is defined as $s_i = 1$, if either ϕ_i at the nodal point or ϕ_i at any one of the four nearest neighboring nodal points is nonzero, and otherwise as $s_i = 0$. The simulations are performed until the substrate (α) is nearly consumed. The overall composition of the system is monitored in time as a measure of numerical accuracy. The changes in the overall composition were on the order of 10^{-4} or less for the runs in this study.

SIMULATION RESULTS AND DISCUSSION

Effect of the Fast GB Diffusion of the IMC Layer

In order to examine the effect of the fast GB diffusion on the growth kinetics of the η-IMC layer, simulations were carried out for two different cases: one taking into account the fast GB diffusion ($\bar{D}_{gb} = 2 \times 10^{-2}$ and $\bar{D}_{\eta} = 2 \times 10^{-5}$) and the other neglecting the fast GB diffusion ($\bar{D}_{gb} = \bar{D}_{\eta} = 2 \times 10^{-4}$). Other than the relative diffusivities $\bar{D}_{gb}$ and $\bar{D}_{\eta}$, the two cases are identical. For both cases, the initial solder composition was equal to the one saturated with Cu, $c_L(\bar{z},0) = c_L^{L\eta}$, and the L/$\eta$ interface energy was taken to be $\sigma_{L/\eta} = 0.1$ J/m^2.

Figure 2 shows a series of snapshots of the temporal evolution of the η-IMC layer for the case with the fast GB diffusion at four different nondimensional times: τ = 1,000, 10,000, 20,000, and 30,000. Each snapshot was obtained by depicting the largest value of ϕ_i (; i = 2,…, N–1) at each nodal point in the gray scale. As the IMC layer grows thicker with time, there is a concurrent coarsening of the η grains, resulting in fewer grains in the IMC layer. Although $\sigma_{gb} > 2\sigma_{L/\eta}$ is assumed, as given in Table II, the liquid solder does not wet the η GBs entirely through the layer, since the driving force for the η phase formation from the diffusion fluxes through the GB is large enough to overcome the difference between σ_{gb} and $2\sigma_{L/\eta}$.

The microstructural evolution of the η-IMC layer depicted in Fig. 2 may be described in terms of a competition between two diffusion processes: (a) the fast GB diffusion to increase the IMC layer thickness and (b) the diffusion driven by the interface curvature effect (i.e., the Gibbs–Thomson effect) to reduce the interface and GB areas. The former provides the initial mass fluxes necessary for η phase growth: the Cu flux to the GB junction with the liquid solder and the Sn flux to the GB junction with the α substrate. The latter distributes the diffusion fluxes from the GB over the η/L and η/α interfaces. Competition between the two diffusion processe determines the groove shapes at the GB junctions. The individual η grains shown in Fig. 2 have a morphology such that the η/L and η/α interfaces have opposite signs of curvature. This is due to the fact that the latter diffusion process is sufficiently fast at the η/L interface but more sluggish at

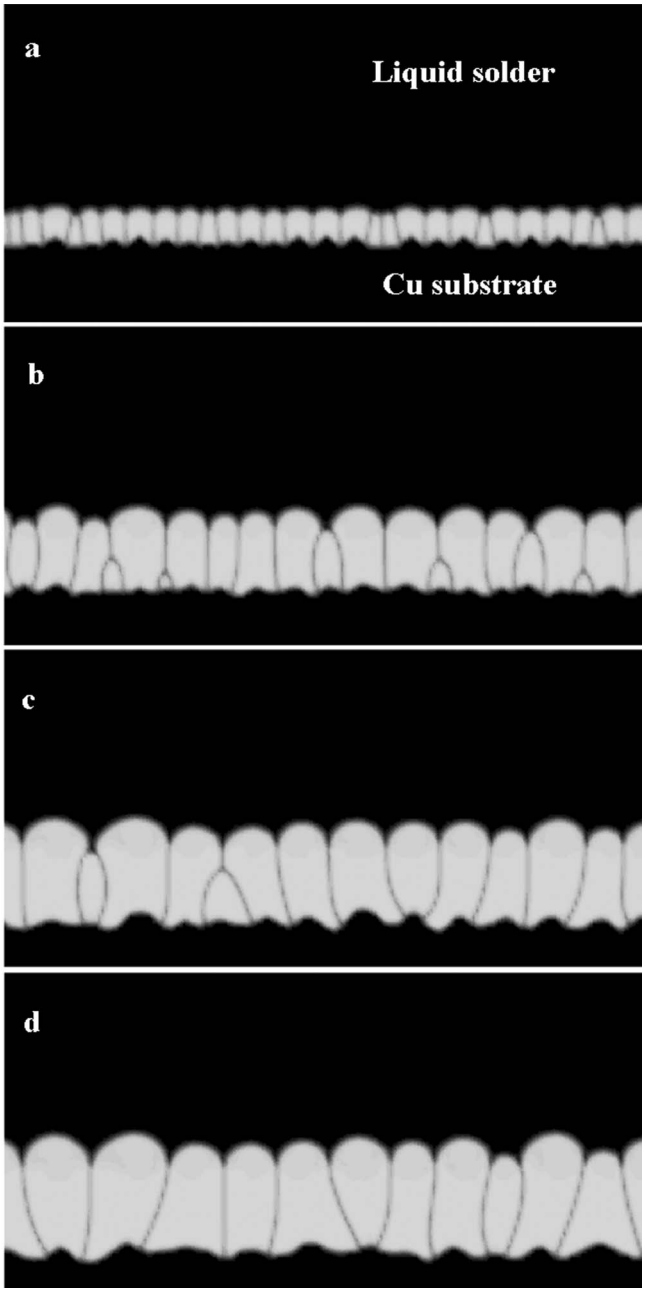

Fig. 2. Microstructural evolution of the η-IMC layer for the case of the fast GB diffusion ($\bar{D}_{gb} = 2 \times 10^{-2}$ and $\bar{D}_{\eta} = 2 \times 10^{-5}$) is depicted for nondimensional times: (a) τ = 1,000, (b) τ = 10,000, (c) τ = 20,000, and (d) τ = 30,000. The initial solder composition was the one saturated with Cu, $c_L(\bar{z},0) = c_L^{L\eta}$. As seen in (b) and (c), the IMC grain coarsening is initiated by the competitive growth of the IMC grains at the solder/IMC interface.

the η/α interface. As can be seen in Fig. 2b and c, the η grain coarsening is initiated by a competitive grain growth at the η/L interface at which the diffusion process caused by the Gibbs–Thomson effect occurs rapidly.

Figure 3 shows the microstructural evolution of the η-IMC layer for the case neglecting the fast GB diffusion. Since the diffusion across the IMC layer is sluggish, the system tends to decrease its energy predominantly by reducing the GB area. Therefore, compared to the case shown in Fig. 2, the liquid solder penetrates deeper into the GB and the η grain coarsening occurs much faster, especially at the early stages of $\tau < 10{,}000$. Because the diffusion distance along the GB is smaller, the GB is still a favorable diffusion path for the IMC layer growth; however, due to its low diffusivity, the growth rate of the IMC layer is much less than in the case with the fast GB diffusion. Consequently, there is less tendency for competitive grain growth, which in turn causes the coarsening rate of the η grains at the late stages of $\tau > 20{,}000$ to be even less than that for the case with the fast GB diffusion.

Figure 4a shows the changes of the (nondimensional) η-IMC layer thickness, $\bar{Z}$, with (nondimensional) time, τ, for the cases with and without the fast GB diffusion. The layer thickness was obtained by dividing the area of the IMC layer by the lateral size (184 h) of the computational cell. The corresponding changes in the number of η grains with time are shown in Fig. 4b.

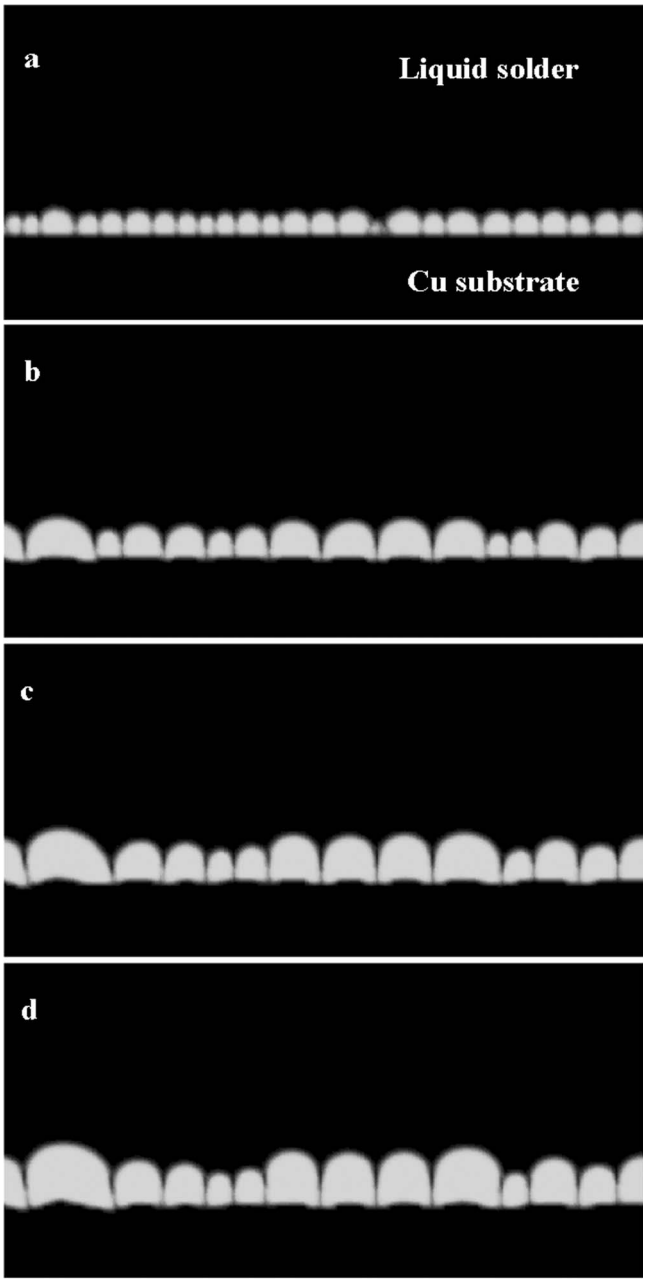

Fig. 3. Microstructural evolution of the η-IMC layer for the case neglecting the fast GB diffusion ($\bar{D}_{gb} = \bar{D}_{\eta} = 2 \times 10^{-4}$) is depicted for nondimensional times: (a) $\tau = 1{,}000$, (b) $\tau = 10{,}000$, (c) $\tau = 20{,}000$, and (d) $\tau = 30{,}000$. Other than the relative GB and bulk diffusivities of the η-IMC layer, $\bar{D}_{gb}$ and $\bar{D}_{\eta}$, the system assumed the same material parameters as those for Fig. 2.

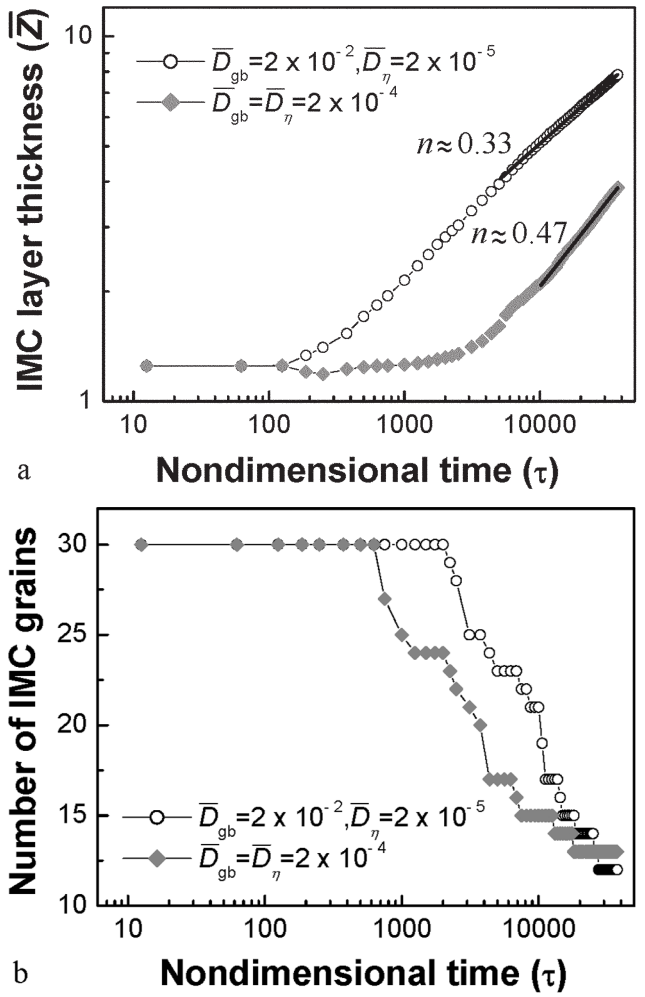

Fig. 4. Changes of (a) the nondimensional thickness of the IMC layer and (b) the number of the IMC grains with nondimensional time are compared between the two cases with and without the fast GB diffusion that correspond to Figs. 2 and 3, respectively. In (a), the temporal growth exponents n were determined in the normal stages of the IMC evolution in which the solder composition increases slightly as the IMC grains coarsen.

Based on the change in the layer thickness shown in Fig. 4a, the evolution of the system from its initial state may be understood by dividing it into three stages, regardless of the presence of the fast GB diffusion. The initial stage of simulation up to $\tau \approx 100$, for which the IMC layer thickness does not change, corresponds to the stage of interface (and GB) broadening. The initial stage is followed by a transient stage in which the GB grooves develop between η grains and the initially flat η/L interface becomes rounded. Thus, in the transient stage, the liquid composition decreases due to the curvature effect at the η/L interface. This is accompanied by the dissolution of η grains into the liquid solder, as shown by the slight decrease in the IMC layer thickness for the case neglecting the fast GB diffusion. At the same time, for the case with the fast GB diffusion, fast diffusion through the broadened GBs takes place so that η grains can grow. Apparently, the grain growth kinetics for the case with the fast GB diffusion is fast enough so that there is a net increase in the IMC layer thickness during this transient stage. The transient stage is then followed by the "normal" stage in which the liquid composition increases slightly as the η grains coarsen. The transient stage ends much earlier for the case with the fast GB diffusion ($\tau \approx 2{,}000$, compared to $\tau \approx 5{,}000$ for the case neglecting the fast GB diffusion) since a part of the Cu flux from the fast GB diffusion enters the liquid solder.

The temporal growth exponent of the IMC layer thickness, n, for $\bar{Z} \propto \tau^n$, was estimated by the least-squares fit of the layer thicknesses in the "normal" stage of simulation. As shown in Fig. 4a, the growth exponent is reduced from $n \approx 0.47$ to $n \approx 0.33$ by taking into account the fast GB diffusion. The exponent $n \approx 0.33$ is well within the experimentally observed range of $0.25 < n < 0.37$.[12–14] This result indicates that, as proposed previously,[13–16] the fast GB diffusion and the reduction rate of the GB density due to the η grain coarsening govern the growth kinetics of the IMC layer during the soldering process.

Effect of the Solder/IMC Interface Energy

In order to examine further the effect of the concurrent coarsening of the η grains on the IMC layer growth kinetics, simulations were carried out with changing the L/η interface energy, $\sigma_{L/\eta}$, while accounting for the fast GB diffusion ($\bar{D}_{gb} = 2 \times 10^{-2}$ and $\bar{D}_{\eta} = 2 \times 10^{-5}$). Figure 5 shows the microstructural evolution of the η-IMC layer when $\sigma_{L/\eta}$ of the system shown in Fig. 2 is changed from 0.1 to 0.05 J/m^2. Because of the lowered value of $\sigma_{L/\eta}$, there is a smaller tendency for competitive grain growth at the L/η interface, compared with the case shown in Fig. 2, and thus the coarsening rate of the η grains is reduced. This in turn results in an increased growth rate of the IMC layer.

The changes in the average IMC layer thickness and the number of η grains with time for the case of $\sigma_{L/\eta} = 0.05$ J/m^2 are compared with those for the case of $\sigma_{L/\eta} = 0.1$ J/m^2 in Fig. 6a and b, respectively. The temporal growth exponent of the IMC layer thickness in the normal stage of simulation is estimated to be $n \approx 0.42$ for the case of $\sigma_{L/\eta} = 0.05$ J/m^2, as indicated in Fig. 6a. Compared to $n \approx 0.33$ for the case of $\sigma_{L/\eta} = 0.1$ J/m^2, the increased value of n by reducing $\sigma_{L/\eta}$ is attributed to the slow coarsening kinetics of the η grains, as shown in Fig. 6b. If the η grain coarsening does not occur at all, and thus the number of η grains remains constant, the exponent

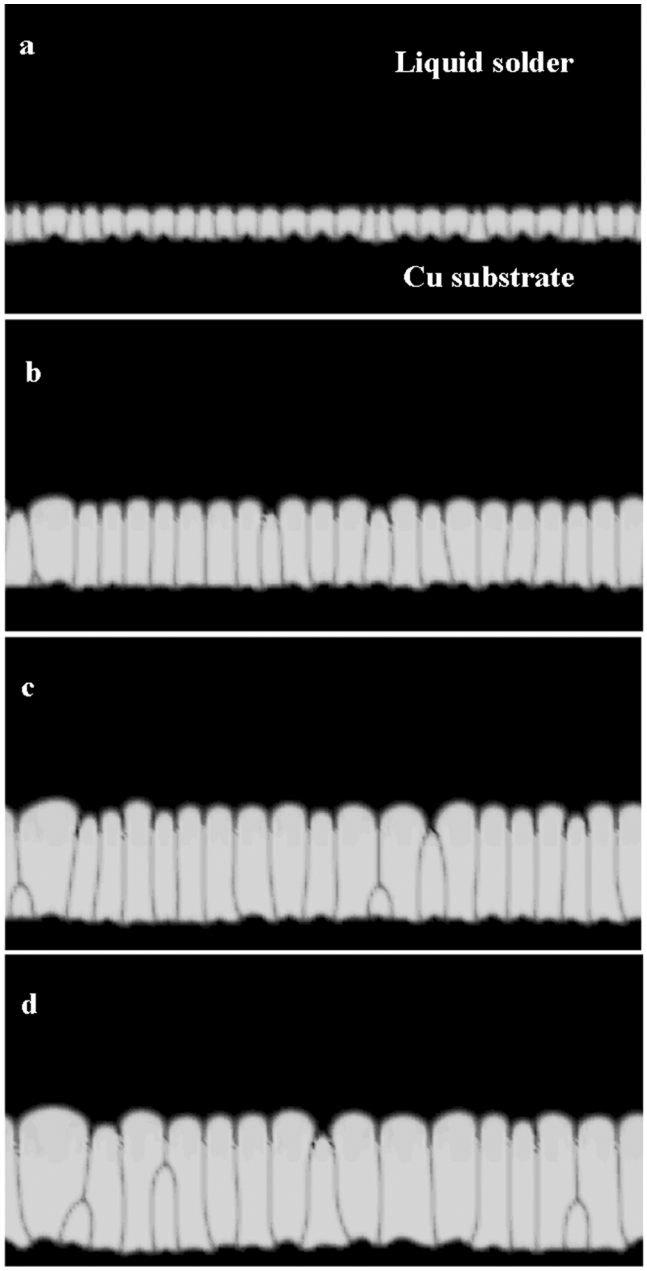

Fig. 5. Microstructural evolution of the η-IMC layer when the solder/IMC interface energy, $\sigma_{L/\eta}$, for the system in Fig. 2 is changed from 0.1 to 0.05 J/m^2: (a) $\tau = 1{,}000$, (b) $\tau = 10{,}000$, (c) $\tau = 20{,}000$, and (d) $\tau = 30{,}000$. By decreasing $\sigma_{L/\eta}$, the competitive growth of the IMC grains at the solder/IMC interface is suppressed and thus the coarsening rate of the IMC grains is reduced.

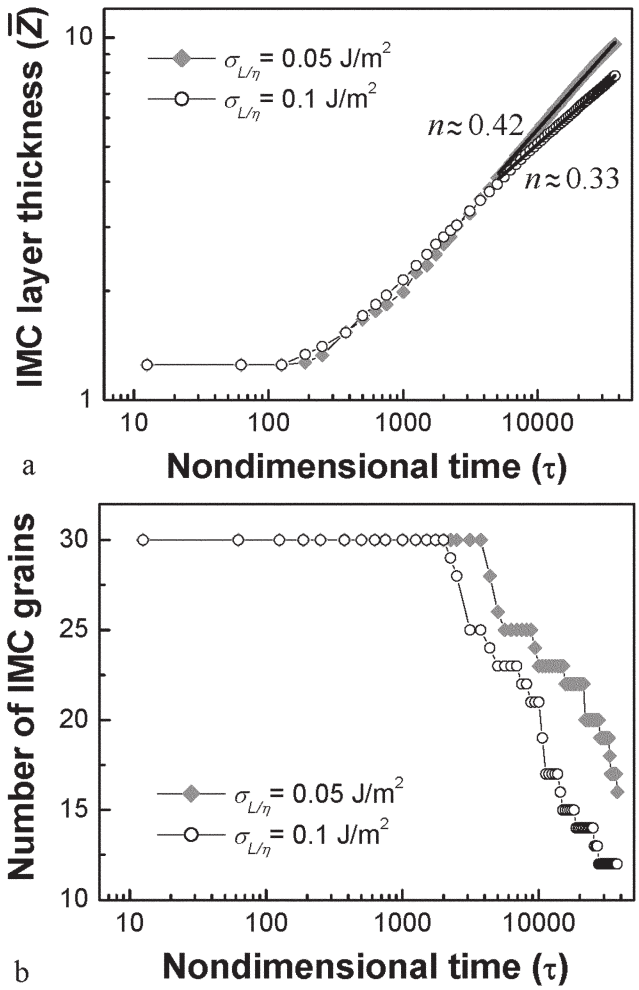

Fig. 6. Changes of (a) the nondimensional thickness of the IMC layer and (b) the number of IMC grains with nondimensional time are compared between the cases of $\sigma_{L/\eta}$ = 0.1 and $\sigma_{L/\eta}$ = 0.05 J/m^2, which correspond to Figs. 2 and 5, respectively.

n will be close to 0.5, as is the case of the parabolic growth law.

Effect of the Initial Cu Content in Solder

Figure 7 shows the microstructural evolution of the η-IMC layer when the initial solder composition of the system in Fig. 2 is changed from $c_L(\bar{z}, 0) = c_L^{L\eta}$ to $c_L(\bar{z},0) = c_L^{L\eta} + 0.02$, which represents nearly pure Sn. The corresponding changes in the IMC layer thickness and the number of the η grains with time are shown in Fig. 8a and b, respectively. Since the initial solder is unsaturated with respect to Cu, dissolution of Cu from the IMC layer and the α substrate occurs at the early stages of soldering. At the same time, the IMC layer grows at the η/α interface due to the Sn flux through the GB in the IMC layer. As a net result of the concurrent dissolution and growth of the IMC layers, the IMC layer thickness decreases at the early stages of soldering, as shown in Fig. 8a. As the liquid solder composition approaches Cu saturation, the dissolution rate slows and the IMC layer thickness starts to grow. Furthermore, as a greater

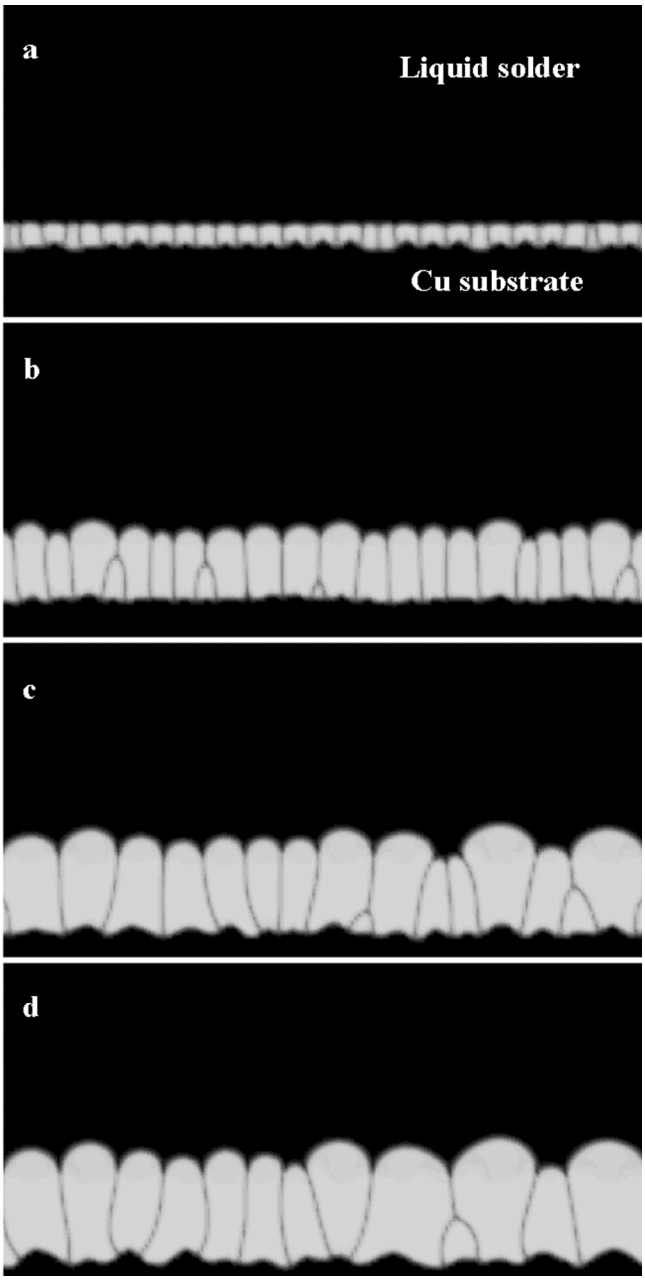

Fig. 7. Microstructural evolution of the η-IMC layer when the initial Sn composition of the solder, $c_L(\bar{z},0)$, for the system in Fig. 2 is increased from $c_L^{L\eta}$ to $c_L^{L\eta}$ + 0.02, corresponding to nearly pure Sn: (a) τ = 1,000, (b) τ = 10,000, (c) τ = 20,000, and (d) τ = 30,000.

portion of the Cu flux by the GB diffusion is incorporated into the IMC formation at the L/η interface, the IMC layer also grows at the L/η interface. The change of the solder composition with time, as measured at the top surface (z_2 = 90 h) of the computational cell, is shown in Fig. 9.

It is worth mentioning that the η grain coarsening is suppressed while the solder is unsaturated with Cu. This is because the Cu flux from the L/η interface into the bulk liquid reduces the composition gradient engendered by the Gibbs–Thomson effect. Therefore, as shown in Fig. 8b, the coarsening rate of the η grains is lowered by using the initially

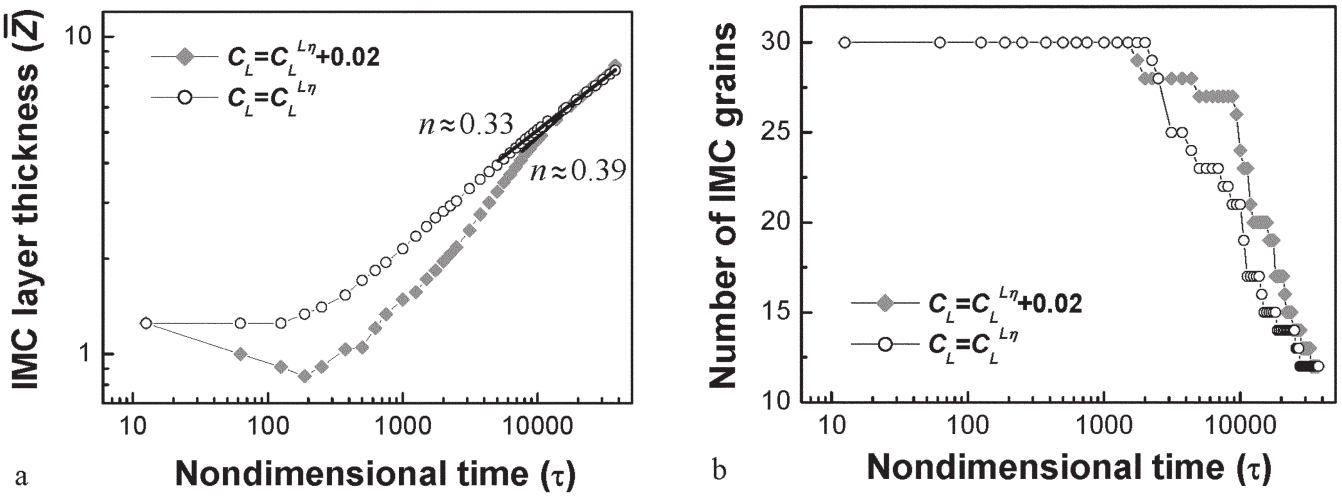

Fig. 8. Changes of (a) the nondimensional thickness of the IMC layer and (b) the number of the IMC grains with nondimensional time are compared between the cases of $c_L(\bar{z},0) = c_L^{L\eta}$ and $c_L(\bar{z},0) = c_L^{L\eta} + 0.02$, which correspond to Figs. 2 and 7, respectively. Note in (a) that there is a crossover in the IMC layer thickness between the two cases at the later stages of IMC growth.

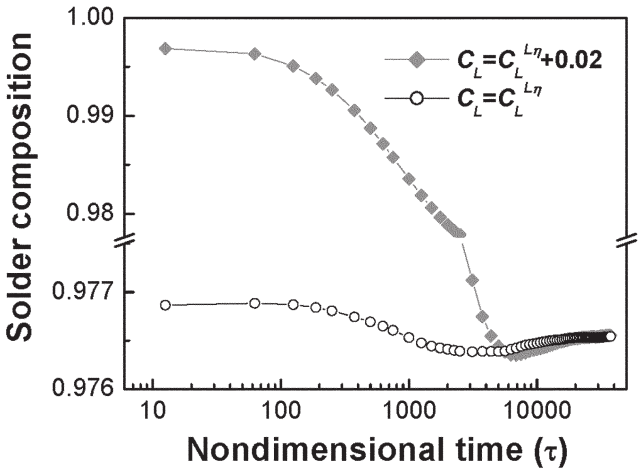

Fig. 9. Change in the solder composition at the top surface (z_2 = 90 h) of the computational cell with nondimensional time is compared between the cases of Cu-saturated ($c_L(\bar{z},0) = c_L^{L\eta}$) and unsaturated ($c_L(\bar{z},0) = c_L^{L\eta} + 0.02$) solders. When the solder is initially unsaturated with Cu, extensive Cu dissolution into the solder occurs at the early stages of soldering. The initial decrease of the solder composition for the case of initially Cu-saturated solder at $\tau < 2{,}000$ is due to the Gibbs–Thomson effect as the initially flat solder/IMC interface becomes rounded.

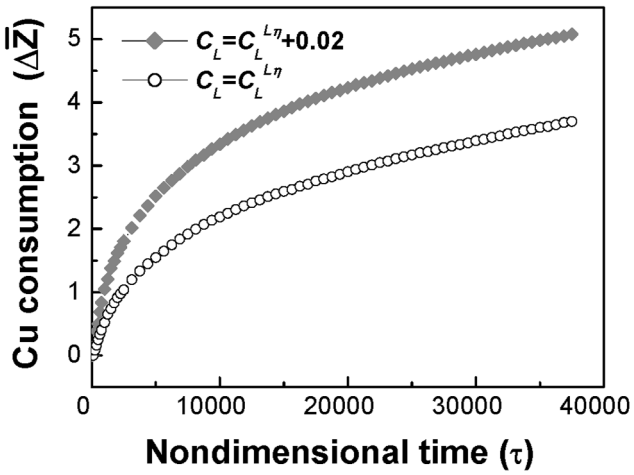

Fig. 10. Consumption of the Cu substrate with nondimensional time is compared for the cases of Cu-saturated ($c_L(\bar{z},0) = c_L^{L\eta}$) and unsaturated ($c_L(\bar{z},0) = c_L^{L\eta} + 0.02$) solders. As expected, the consumption rate of the Cu substrate is much higher for the case of unsaturated solder.

unsaturated solder. Consequently, this lowered coarsening rate is responsible for the IMC layer thickness being even greater for the case of the nearly pure Sn solder than for that of the Cu-saturated solder at the later stages of soldering, as shown in Fig. 8a by the crossover in the layer thickness between the two cases. The temporal growth exponent is accordingly increased from $n \approx 0.33$ for the saturated solder to $n \approx 0.39$ for the nearly pure Sn solder. This simulation result is in qualitative agreement with the experimental result by Schaefer et al.[14] of $n = 0.25$ and $n = 0.37$ for Sn-36Pb-2Ag solders with and without Cu saturation, respectively.

Figure 10 compares the consumption of the Cu substrate, $\Delta\bar{Z}$, with the nondimensional soldering time for the cases of Cu-saturated and nearly pure Sn solders. As expected, the consumption rate of the Cu substrate during soldering was reduced by using the Cu-saturated solder. Finally, we note that, although the detailed numbers, such as the temporal growth exponents, depend on the initial condition, such as the number and size distribution of the IMC grains, and the material parameters, the simulation results in this section present a generic picture for the effect of the fast GB diffusion on the growth evolution of the η-IMC layer during soldering reactions.

SUMMARY

The microstructural and growth evolution of the IMC (Cu_6Sn_5) layer formed during reflow soldering with Sn-Cu solder alloys on a Cu substrate was simulated using a multiphase field model. The

multiphase field simulation accounted for the fast GB diffusion in the IMC layer, the concurrent coarsening of the IMC grains along with the IMC layer growth, and the dissolution of Cu from the substrate and IMC layer. The microstructural evolution of the IMC layer could be described in terms of the competition between two diffusion processes: the fast GB diffusion to thicken the IMC layer and the diffusion driven by the Gibbs–Thomson effect to reduce the interface area.

The simulation results supported the previous suggestion that the growth kinetics of the IMC layer thickness (W), following $W \propto t^n$ with n about 1/3, is governed by the fast GB diffusion and the concurrent coarsening rate of the IMC grains. The IMC grain coarsening is initiated by a competitive growth of the IMC grains at the solder/IMC interface. The simulation also showed, in accordance with previous experimental observation, that the temporal growth exponent of the IMC layer thickness is lowered by increasing the initial Cu content in the solder to its saturation level. This is because the dissolution of Cu into an unsaturated solder reduces the coarsening rate of the IMC grains and thereby increases the temporal growth exponent to a value closer to 0.5, as in the case of the parabolic growth law.

ACKNOWLEDGEMENTS

The authors are grateful to Professor S.G. Kim, Kunsan National University, for the valuable discussions. This work was supported by Grant No. KRF-99-041-E00484 from the Korea Research Foundation.

REFERENCES

1. M. Abtew and G. Selvaduray, *Mater. Sci. Eng. R* 27, 95 (2000).
2. K.N. Tu and K. Zeng, *Mater. Sci. Eng. R* 34, 1 (2001).
3. D.R. Frear and P.T. Vianco, *Metall. Mater. Trans. A* 25A, 1509 (1994).
4. D. Yao and J.K. Shang, *Metall. Mater. Trans. A* 26A, 2677 (1995).
5. P.L. Tu, Y.C. Chan, K.C. Hung, and J.K.L. Lai, *Scripta Mater.* 44, 317 (2001).
6. C.K. Shin, Y.J. Baik, and J.Y. Huh, *J. Electron. Mater.* 30, 1323 (2001).
7. H.K. Kim and K.N. Tu, *Appl. Phys. Lett.* 67, 2003 (1995).
8. A.A. Liu, H.K. Kim, K.N. Tu, and P.A. Totta, *J. Appl. Phys.* 80, 2774 (1996).
9. S.K. Kang, R.S. Rai, and S. Purushothaman, *J. Electron. Mater.* 25, 1113 (1997).
10. A.J. Sunwoo, J.W. Morris, Jr., and G.K. Lucey, Jr., *Metall. Trans. A* 23A, 1323 (1992).
11. W.K. Choi and H.M. Lee, *J. Electron. Mater.* 29, 1207 (2000).
12. S. Bader, W. Gust, and H. Hieber, *Acta Metall. Mater.* 43, 329 (1995).
13. H.K. Kim, H.K. Liou, and K.N. Tu, *Appl. Phys. Lett.* 66, 2337 (1995).
14. M. Schaefer, W. Laub, R.A. Fournelle, and J. Liang, *Design and Reliability of Solders and Solder Interconnections,* ed. R.K. Mahidhara, D.R. Frear, S.M.L. Sastry, K.L. Murry, P.K. Liaw and W. Winterbottom (Warrendale, PA: TMS, 1997), p. 247.
15. H.K. Kim and K.N. Tu, *Phys. Rev. B* 53, 16027 (1996).
16. M. Schaefer, R.A. Fournelle, and J. Liang, *J. Electron. Mater.* 27, 1167 (1998).
17. I. Steinbach and F. Pezzolla, *Physica D* 134, 385 (1999).
18. S.G. Kim, W. T. Kim, T. Suzuki, and M. Ode, *J. Cryst. Growth* 261, 135 (2004).
19. D.N. Bhate, A. Kumar, and A.F. Bower, *J. Appl. Phys.* 87, 1712 (2000).
20. S.G. Kim, W.T. Kim, and T. Suzuki, *Phys. Rev. E* 60, 7186 (1999).
21. F. Larché and J.W. Cahn, *Acta Metall.* 33, 331 (1985).
22. M. Onishi and H. Fujibuchi, *Trans. Jpn. Inst. Met.* 16, 539 (1975).
23. Z. Mei, A.J. Sunwoo, and J.W. Morris, Jr., *Metall. Trans. A* 23A, 857 (1992).
24. P.T. Vianco, A.C. Kilgo, and R. Grant, *J. Electron. Mater.* 24, 1493 (1995).
25. J.H. Shim, C.S. Oh, B.J. Lee, and D.N. Lee, *Z. Metallkd.* 87, 205 (1996).